Electrical Conductivity of Multiphase Garnet under High-Temperature and High-Pressure Conditions

Kui Han [*1, 2], **Xinzhuan Guo**[3], **Hanyong Liu**[4], **Fengbao Ji**[5]

1. *Key Laboratory of Earth Exploration and Information Techniques* (*Chengdu University of Technology*), *Ministry of Education, Chengdu 610059, China*
2. *Bayerisches Geoinstitute, University of Bayreuth, Bayreuth D95447, Germany*
3. *CAS Key Laboratory of High-Temperature and High-Pressure Study of the Earth' Interior, Institute of Geochemistry, Chinese Academy of Sciences, Guiyang 550081, China*
4. *State Key Laboratory for Mineral Deposits Research, School of Earth Sciences and Engineering, Nanjing University, Nanjing 210023, China*
5. *Tibet Museum of Natural Science, Lhasa 850000, China*

Kui Han: https://orcid.org/0000-0001-5111-6642

ABSTRACT: Mineral mixing, a fundamental process during mantle convection, alters the chemical composition of mantle minerals. However, the impact of this process on the electrical conductivity of mineral assemblages remains poorly understood. We measured the electrical conductivity of three single-phase garnets and their corresponding mixtures at 1.5 GPa and varying temperatures using the impedance spectroscopy within frequency from 10^{-1} to 10^{6} Hz. The electrical conductivity of dehydrated garnets is primarily controlled by their iron content, exhibiting an activation energy about 1.0 eV, indicative of small polaron conduction. The garnet mixture displays lower electrical conductivities and higher activation energies compared to their single-phase counterparts. This discrepancy of conductivity can be half order of magnitude at high temperatures (>1 073 K), suggesting formation of resistive grain boundaries during the mixing process. In the mantle transition zones, grain boundary conductivity could exert a limited impact on the bulk conductivity of the interface between the stagnant slab and ambient mantle.
KEY WORDS: almandine, impedance spectroscopy, interface, conductivity anomalies, garnets, minerals.

0 INTRODUCTION

The Earth's mantle exhibits significant heterogeneity with distinct lithology and chemical compositions, a consequence of early differentiation and ongoing geological events (Liu et al., 2022; van Keken, 2002). Magnetotelluric and geomagnetic observations are a powerful tool in probing this heterogenous structure because electrical conductivity of minerals and rocks is sensitive to their chemical composition (Zhang X B et al., 2023; Zhang J et al., 2022; Zhang and Yoshino, 2016; Hu et al., 2013; Dai et al., 2012). Mantle rocks undergo mechanical and chemical mixing under specific thermochemical conditions, which can occur over extended geological timescales, potentially reaching billions of years (Stixrude and Lithgow-Bertelloni, 2012; Holzapfel et al., 2005). This process not only modifies the bulk chemical composition but also changes grain boundary structures and chemistry (Linckens and Tholen, 2021; Marquardt and Faul, 2018). In the mixed aggregates of diopside

and olivine, incompatible ions segregate to grain boundaries (Hiraga et al., 2004). Grain boundary conduction was suggested to occur in the albite-orthoclase mixture, enhancing the bulk conductivity of feldspar solid solutions (Han et al., 2021). The grain boundary could play an important role in the conductivity of a rock, as observed in several natural and synthetic rocks (Pommier et al., 2018; Hui et al., 2015; Farla et al., 2010; Dai et al., 2008; Roberts and Tyburczy, 1991). Despite the potential influence of grain boundaries, few studies have investigated how the mixing process of mantle minerals affects rock conductivity. Therefore, understanding this impact is crucial for interpreting the chemical composition and mixing history of the mantle using magnetotelluric and geomagnetic data.

Garnet, a major mineral in both the crust and mantle, comprises two solid solution series with six endmembers (Wood et al., 2013). In metamorphic and igneous rocks, garnet often shows chemical zoning due to the slow diffusion of elements, characterizing various geological processes (Li et al., 2023; Yu et al., 2023; Zhou and Song, 2023; Luo et al., 2022; Nagurney et al., 2021). The garnet transformed from basalt in the subducted oceanic plates has a distinct chemical composition from that in the ambient mantle (Wood et al., 2013). Therefore, garnet could be a good mineral for the investigation on the effect of mineral mixing on electrical conductivity. The electrical con-

ductivity of garnet is affected by its chemical composition, as demonstrated by an increase in conductivity when the Fe/(Fe + Mg) ratio increases (Romano et al., 2006). Hydrogen, the primary charge carrier in hydrous garnet, could enhance the conductivity of garnet (Liu et al., 2019; Dai and Karato, 2009). In anhydrous conditions, the conduction mechanism of garnet transitions from small polaron (electric hoping between Fe^{2+} and Fe^{3+}) to vacancies as Mg content increases (Romano et al., 2006). Previous research has mainly focused on measuring the electrical conductivity of single-phase garnet. While studies have shown that Fe-Mg interdiffusion between pyrope and almandine can induce the diffusion of Fe^{2+} and Mg^{2+} along grain boundaries (Zhang et al., 2019), the impact of such garnet mixing on the electrical conductivity of mantle rocks remains largely unexplored.

Electrical conductivities were measured for three single-phase garnets and their corresponding mixtures at varying temperatures and a confining pressure of 1.5 GPa. The mixture samples exhibited lower conductivities and higher activation energy compared to their single-phase counterparts. This observation is likely attributable to the presence of resistive grain boundaries formed during the mixing process.

1 METHODS

1.1 Starting Materials

Three natural garnets with distinct chemical compositions were used as starting materials: SD (Songduo, Tibet Plateau), LYG (Lianyungang, Jiangsu Province), and XJ (Altay, Xinjiang Autonomous Region). SD was handpicked from an eclogite, while LYG and XJ were megacrysts. Chemical compositions were determined using an electron microscope at Chengdu University of Technology (China) with an accelerating voltage of 15 kV and a beam current of 20 nA. As shown in Table 1, XJ ($Alm_{70}Py_{17}Grs_4Sps_8$) has the highest spessartine, while SD ($Alm_{47}Py_{20}Grs_{31}Sps_2$) has the most grossular and lowest almandine content. All samples were ground to a powder (with the grain size <10 μm) and heated at 1 273 K for 12 hours in a H_2 atmosphere to remove structural water in crystal lattice. Two-phase mixtures of $LYG_{50}XJ_{50}$, $LYG_{66}SD_{34}$, and $LYG_{50}SD_{50}$ (wt.%) were prepared by mechanical mixing. Dehydrated single-phase

garnets and mixtures were then cold-pressed into 3 mm diameter pellets with a thickness of approximately 1.3 mm for subsequent electrical conductivity measurements.

1.2 Electrical Conductivity Measurements

Garnet samples were loaded into nickel (Ni) capsules lined with boron nitride (BN) for electrical insulation. Platinum (Pt) discs served as electrodes on both ends of the samples. To buffer oxygen fugacity, Ni/NiO powder was added atop the Pt working electrode. A graphite furnace within a piston cylinder apparatus (Nanjing University, China) provided high-pressure and high-temperature conditions (detailed assembly in Liu et al., 2023). During the initial heating stage, samples were hot-pressed at 873 K for 2 hours to remove any absorbed moisture from the assembly.

Impedance spectroscopy was collected using the AMETEK® Solartron 1296 impedance gain-phase analyzer. An AC voltage with an amplitude of 1 V and a frequency sweep from 0.1 to 10^6 Hz was employed. At least one circle, including two heating and one cooling, was collected for all samples at 1.5 GPa and 573–1 273 K. The total measurement duration at high temperatures was limited to less than one hour, consistent with previous findings by Yang and McCammon (2012) indicating negligible iron loss for short measurement times (~2 min per analysis) at lower temperatures (<1 273 K). Impedance spectra were only collected after achieving a stable resistance at each temperature, ensuring a steady thermal state. Equivalent circuits comprising of a resistor and a constant phase element in parallel was used to fit the impedance spectra. Following the measurements, sample dimensions were recalibrated by measuring the effective thickness of recovered sample as well as the contacting surface area between sample and electrodes. The electrical conductivity (σ) was calculated using the formula $\sigma = l/S \cdot R$, where l represents the sample thickness, S represents the surface area, and R represents the fitted resistance value. The overall uncertainty associated with the electrical conductivity measurements is less than 5%.

1.3 Water Content

Fourier transform infrared (FTIR) spectroscopy was em-

Table 1 The chemical composition (wt.%) of garnet samples

Sample	SD	LYG	XJ
Na_2O	0.01 (1)	0.02 (1)	0
MgO	5.11 (46)	4.43 (18)	4.42 (17)
Al_2O_3	21.59 (31)	21.22 (13)	21.13 (14)
SiO_2	40.43 (71)	39.02 (59)	37.96 (64)
K_2O	0	0.01 (1)	0.01
CaO	10.99 (45)	1.74 (7)	1.25 (6)
TiO_2	0.08 (1)	0	0.01 (1)
Cr_2O_3	0.02 (3)	0	0.03 (1)
MnO	0.68 (15)	1.01 (14)	3.68 (11)
FeO	21.31 (67)	32.68 (47)	32.09 (3)
Total	100.21	100.13	100.56
Formular	$(Fe_{1.4}Mg_{0.6}Ca_{0.9}Mn_{0.1})Al_2(SiO_4)_3$ $Al_{47}Py_{20}Gr_{31}Sp_2$	$(Fe_{2.2}Mg_{0.5}Ca_{0.2}Mn_{0.1})Al_2(SiO_4)_3$ $Al_{75}Py_{18}Gr_5Sp_2$	$(Fe_{2.1}Mg_{0.5}Ca_{0.1}Mn_{0.3})Al_2(SiO_4)_3$ $Al_{70}Py_{17}Gr_4Sp_8$

ployed to determine the water content of the samples. Since a considerable amount of water can be inevitably absorbed by the powder sample, leading to an artifactual error (Keppler and Rauch, 2000), the water content of samples was not measured before conductivity measurements. Instead, it was only measured after the electrical conductivity measurements. Each sample was double-side polished and dried for over 12 hours at 400 K prior to the FTIR measurements. FTIR analysis was performed using a Bruker Vertex 70V FTIR spectrometer coupled with a Hyperion 2000 microscope (Bayerisches Geoinstitut, Germany). The aperture was 100 μm, which gives a spot size of 60 μm × 60 μm. 128 scans were collected for each specimen at 4 cm^{-1} resolution. The spectra between 2 000 to 10 000 cm^{-1} were collected, and those from 3 000 to 4 000 cm^{-1} were analyzed because of its sensitivity to the vibration of hydrogen-related species (Bell et al., 1995). The modified Beer-Lambert law was used to determine the concentration of water in the lattice, $A = I \cdot c \cdot t \cdot \gamma$, where A denotes total integral absorbance, I is integral molar coefficient of absorption, c refers to the content of water, t is sample thickness, and γ stands for the orientation factor. The absorbance between the wavenumber of 3 000 and 3 750 cm^{-1} was integrated. γ in our study was assumed to be 1/3 due to the random orientation in polycrystalline garnet (Geiger and Rossman, 2018).

2 RESULTS

Figure 1 shows the FTIR spectra of each sample after the impedance spectroscopy experiment. No peaks attributable to structural water (OH^-) were observed. The absence of the characteristic peak for almandine-rich garnets around 3 623–3 630 cm^{-1} (Geiger and Rossman, 2018) further confirms negligible water content in the samples. The broad peak observed around B395 and B386 likely stems from the background signal.

Impedance spectroscopy revealed suppressed semi-circle patterns in the complex impedance spectra of the garnet samples (Figure 2). A small semi-circle observed at low frequencies in some spectra is likely associated with grain boundary conduction (Farla et al., 2010). At high temperatures, a single semi-circle could indicate either dominant conduction within the grain interiors or overlapping contributions from both grain interiors and grain boundaries with similar relaxation times.
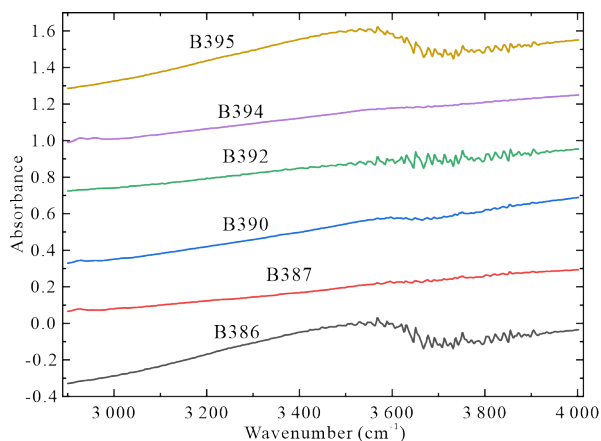
The electrical conductivities of all samples were determined across a range of temperatures and plotted as a function of reciprocal temperature ($1/T$) in Figure 3. This data was fitted to the Arrhenius equation as follows

$$\sigma = A \exp(-\Delta H/kT) \tag{1}$$

where A is the pre-exponential factor, ΔH is the activation energy, k is the Boltzmann constant, and T is the absolute temperature. The resulting activation enthalpy and pre-exponential factor for the samples are listed in Table 2.

The electrical conductivities of single-phase garnets were measured over one cycle, while those of garnet mixtures were measured over 2 cycles (Figure 3). The electrical conductivity at the first heating stage could be affected by moisture in the assembly. After the first heating stage, both the single-phase and mixture samples exhibited consistent conductivity behavior across their respective heating and cooling cycles. The linear relationship between reciprocal temperature and conductivity observed for SD (Figure 3a) suggests a constant conduction mechanism throughout the temperature range. LYG, XJ, and their mixture ($LYG_{50}XJ_{50}$) displays a variation in slope with increasing temperature (Figures 3b and 3d), implying a shift in the dominant conduction mechanism at higher temperatures compared to lower temperatures. Their conductivities at higher temperatures (>900 K) were fitted to the Arrhenius equation to obtain the pre-exponential factor and activation energy listed in Table 2.

Among the single-phase garnets, SD exhibits a slightly higher conductivity compared to LYG, while LYG and XJ possess similar conductivities at high temperatures (>1 000 K). The activation energy of SD (0.89 eV) is slightly lower than both XJ (0.97 eV) and LYG (1.05 eV), despite the lower iron content SD (X_{Fe} = 0.46) compared to LYG (0.73) and XJ (0.70). Notably, the conductivities of both SD and LYG are higher than their mixtures (Figure 3c). Similarly, LYG and XJ show higher conductivities than their mixture, $LYG_{50}XJ_{50}$, and the discrepancy is about half order of magnitude lower than its con-

Figure 1. Representative FTIR spectra of garnet samples after electrical conductivity measurements.
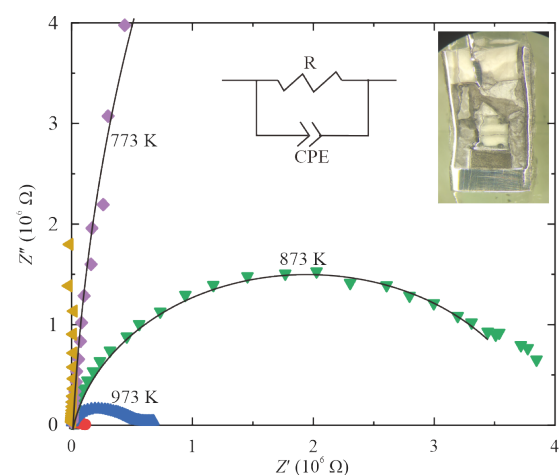

Figure 2. Representative complex impedance spectra of the LYG sample, showing real and imaginary impedance components. Low-frequency data points with high scatter were excluded. The semi-circular spectra were simulated by an equivalent circuit including a resistor (R) and a constant phase element (CPE) in parallel (inset) photomicrograph of the recovered cell assembly.
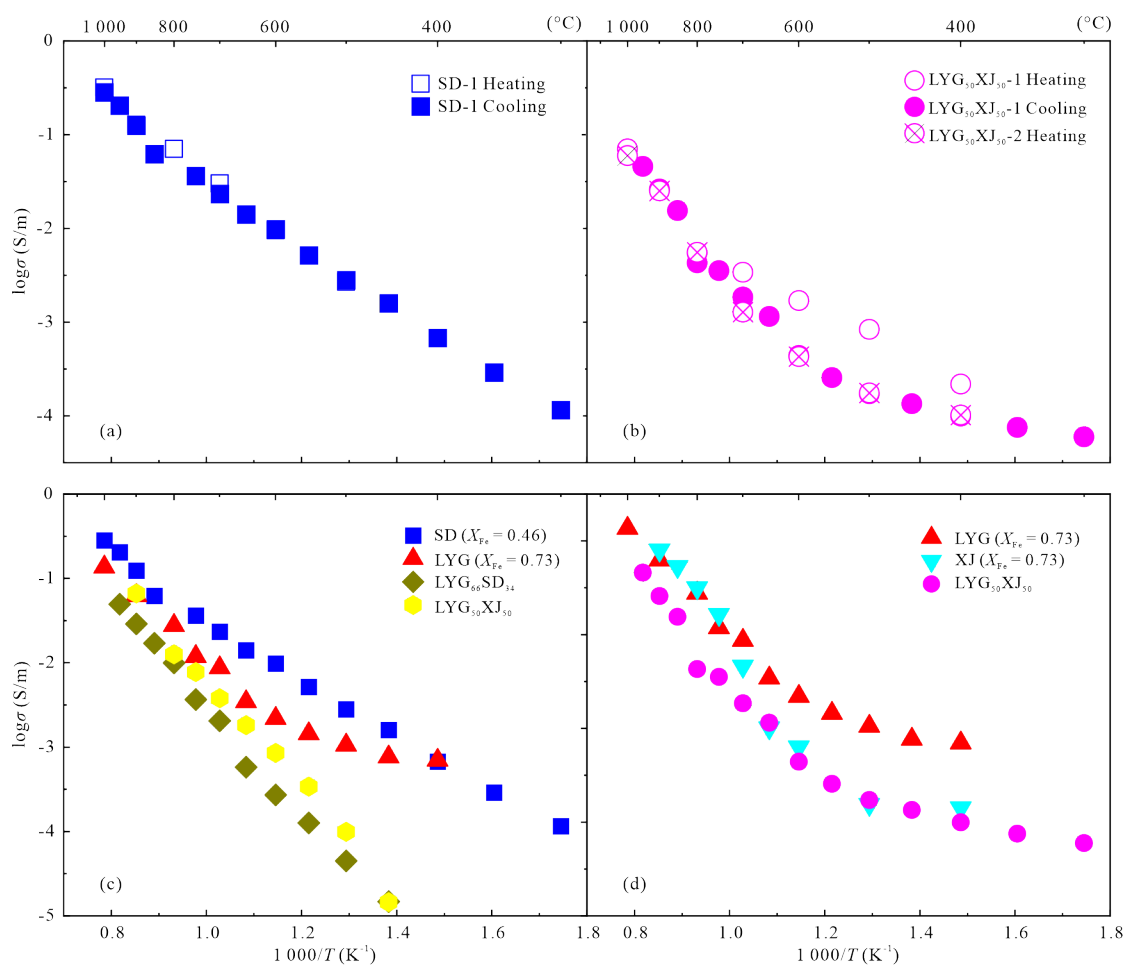
Figure 3. Electrical conductivity of single-phase (a) and mixed-phase (b) garnets plotted as a function of reciprocal temperature ($1\,000/T$). Panels (c) and (d) compared the conductivity of the single-phase samples with their corresponding mixtures during the cooling cycle data. XJ was only collected during a single heating cycle (d) due to a thermocouple failure at 1 173 K.

Table 2   Summary of runs

Runs	Samples	X_{Fe}*	Pressure (GPa)	Temperature (K)	σ_0	ΔH (eV)	Comments
B386	SD	0.46	1.5	573–1 273	2 621	0.89	Single phase
B387	LYG	0.73	1.5	573–1 273	1 192	1.05	Single phase
B395	XJ	0.70	1.5	573–1 173	1 507	0.97	Single phase
B390	$LYG_{50}XJ_{50}$	0.72※	1.5	573–1 273	1 632	1.23	Mixture
B392	$LYG_{66}SD_{34}$	0.64※	1.5	573–1 273	3 533	1.41	Mixture
B394	$LYG_{50}SD_{50}$	0.59※	1.5	573–1 173	12.56	1.27	Mixture

*X_{Fe} denotes the mole fraction of iron in metal ions (X_{Fe} = Fe/Σ(Fe + Mg + Mn + Ca); ※is calculated based on the weight percentage of each constituents in the mixture.

stituent single phases at 1 223 K (Figure 3d). This discrepancy increases with decreasing temperature due to the distinct conduction mechanisms between high and low temperature ranges. Furthermore, as shown in Table 2, the activation energies for electrical conduction in the mixed-phase garnets are consistently higher than those in the single-phase counterparts.

Post-experiment observations revealed evidence of exsolution in some SD garnet samples. This exsolution is manifested as the formation of a myrmekitic texture within both the single-phase garnet (B386) (presented in the ESM Figure S1) and the two-phase mixture (B394) (Figure 4). Myrmekitic texture is

characterized by the unmixing of domains enriched in Ca^{2+} and depleted in Fe^{2+} and Mg^{2+}, accompanied by a corresponding shift in the abundance of Al^{3+} and Si^{4+} (ESM Figure S2 and Table S1). Scanning electron microscopy (SEM) analysis did not detect significant interdiffusion of Fe^{2+} and Ca^{2+} between the distinct garnet phases. This observation aligns well with the established low interdiffusion coefficients reported for Fe^{2+}/Mg^{2+} ($10^{-16.36}$ m^2/s) and Ca ($10^{-16.23}$ m^2/s) at experimental conditions of 1 000 °C and 1.5 GPa (Freer and Edwards, 1999). Given these diffusion coefficients, the estimated maximum diffusion length for Fe^{2+}/Mg^{2+} and Ca^{2+} would be approximately 0.2 µm.
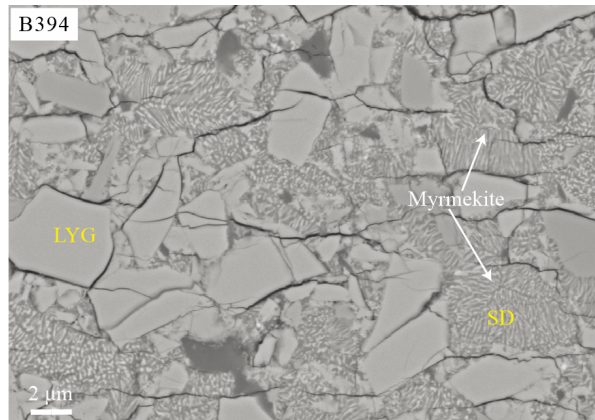
Figure 4. Backscatter electron (BSE) image of the mixed-phase sample (B394) showing myrmekitic texture development within SD garnet grains to varying degrees.

3 DISCUSSION

3.1 Electrical Conductivity of Single-Phase Garnet

The electrical conductivity of garnet is affected by water content, iron content and $Fe^{3+}/\Sigma Fe$ ratio, besides oxygen fugacity and temperature and pressure. Water can significantly increase the conductivity of garnet via the dominant conduction mechanism-proton (H^+) (Feng and Guo, 2022; Liu et al., 2019; Dai et al., 2012; Dai and Karato, 2009). In the present study, the effect of water on the garnet conductivity could be ruled out because the garnet samples are almost dry. Romano et al. (2006) demonstrated a positive correlation between electrical conductivity and total iron content in a series of garnets, a trend also observed in other mantle minerals (Zhang and Yoshino, 2016; Yoshino et al., 2012). However, the reported conductivity variation for $Al_{43}Py_{56}Gr_1$ and $Al_{76}Py_{20}Gr_4$ is only 0.2 order of magnitude (Dai et al., 2012). For a constant iron content, the conductivity of garnet could be affected by $Fe^{3+}/\Sigma Fe$ as observed in augite (Yang and McCammon, 2012). Despite a lower total iron content in SD ($X_{Fe} = 0.46$) compared to LYG ($X_{Fe} = 0.73$) and XJ ($X_{Fe} = 0.7$), the conductivities of the three single-phase garnets are comparable at high temperature. This observation might be attributed to a potentially higher ferric iron content in the SD garnet.

The formation of myrmekitic texture appears to have minimal impact on the electrical conductivity of the SD garnet samples. The miscibility gap between grossular and pyrope is known to be compositionally dependent (Dachs, 2006). The higher mole fraction of grossular (0.45) in the SD garnet results in a significantly higher solvus temperature (1 200 °C) compared to the lower grossular content observed in LYG (0.07) and XJ (0.03) exhibiting much lower solvus temperatures of less than 400 °C (Dachs, 2006).

During exsolution in SD, Fe (Mg)-rich and Ca-rich endmembers become segregated, leading to a redistribution of elements within the mineral lattice. However, this process typically has minimal impact on the bulk chemical composition of each mineral, including the iron content. Consequently, the influence of the myrmekitic texture on the conductivity of both the SD garnet and the mixture is likely negligible (Romano et al., 2006). This aligns with observations by Wang et al. (2014)

who reported a negligible influence of exsolution on the conductivity of myrmekitic K-feldspar up to 1 000 °C.

The electrical conductivities of our single-phase garnets were compared with those reported in previous studies (Figure 5). The observed conductivities in our study are approximately one order of magnitude higher than those reported for the dry garnet ($Al_{14}Py_{73}Grs_{13}$) by Dai and Karato (2009) and about half order of magnitude higher than the nearly "dry" garnet ($Al_{55}Py_{27}Gr_{27}Sp_2$) at high temperature (>1 073 K) reported by Liu et al. (2019). These difference can be attributed to the higher iron content in our samples. By contrast, Romano et al. (2006) reported significantly higher conductivity of $Al_{80}Py_{20}$ and Al_{100} garnets compared to our LYG ($Al_{75}Py_{18}Grs_5Sp_2$) and XJ ($Al_{70}Py_{17}Gr_4Sp_8$), despite similar iron contents. This discrepancy is likely due to the presence of uncharacterized structural water in their samples, as the water content was not reported. Alternatively, the higher pressure (10 GPa) used in their study compared to ours (1.5 GPa) could be a contributing factor, as Romano et al. (2006) suggested a negative correlation between conductivity and the increasing pressure.

The conductivities of all studied garnets exceed that of the assemblage of ilmenite and garnet previously reported by Xu and Shankland (1999). However, the unknown exact proportion of garnet within this assemblage hinders a precise evaluation of its contribution to the bulk conductivity (Xu and Shankland, 1999). Dai et al. (2012) reported a lower conductivity for a dry garnet ($Py_{20}Al_{76}Grs_4$) compared to ours despite similar ion content. This observation may be related to differing oxygen

- – – Ilmenite + garnet, Xu and Shankland (1999)
- · · · $Al_{80}Py_{20}Gr_0Sp_0$, Romano et al. (2006)
- — $Al_{100}Py_0Gr_0Sp_0$, Romano et al. (2006)
- – · – $Al_{14}Py_{73}Gr_{13}Sp_0$ (dry), Dai and Karato (2009)
- – – $Al_{14}Py_{73}Gr_{13}SP_0$ (465 ppm), Dai et al. (2012)
- · · · · · $Al_{76}Py_{20}Gr_4Sp_0$ (dry), Dai et al. (2012)
- – · – $Al_{55}Py_{27}Gr_{15}Sp_2$ (dry), Liu et al. (2019)
- ■ $Al_{75}Py_{18}Gr_5Sp_2$ (B387)
- ◆ $Al_{47}Py_{20}Gr_{31}Sp_2$ (B386)
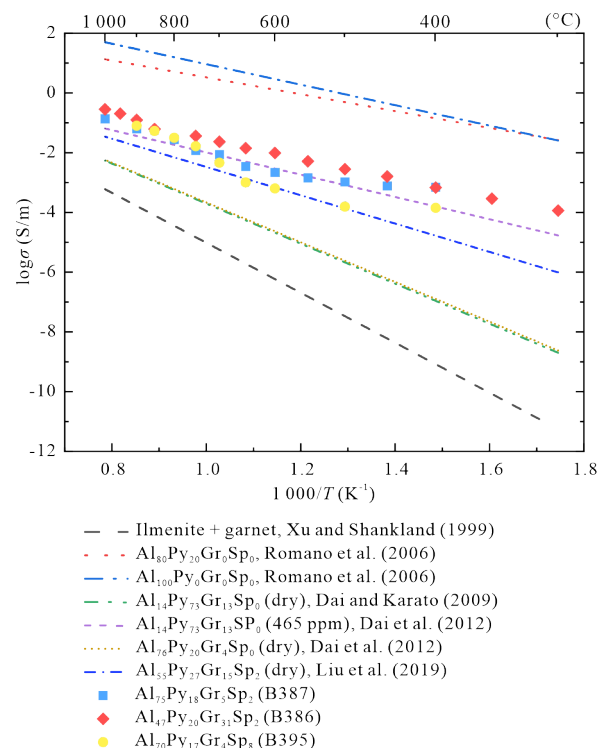- ● $Al_{70}Py_{17}Gr_4Sp_8$ (B395)

Figure 5. Comparison of the electrical conductivity of the single-phase garnets from this study with data reported in previous studies. Conductivity data for $Al_{80}Py_{20}Gr_0Sp_0$ and $Al_{100}Py_{20}Gr_0Sp_0$ from Romano et al. (2006) at 573–873 K and 10 GPa were adjusted for high-temperature comparison through extrapolation.

fugacities, which can influence the $Fe^{3+}/\Sigma Fe$ ratio. As conductivity increases with increasing oxygen fugacity (Amulele et al., 2022; Dai et al., 2012), the lower IM (Fe-Fe_3O_4) buffer used in their study compared to the Ni-NiO buffer employed in ours likely explains the discrepancy.

3.2 Conduction Mechanism

The electrical conduction mechanism in garnet appears to differ between low and high temperatures. This is evidenced by the significantly lower activation energies observed for LYG and XJ at low temperatures (<900 K) compared to high temperatures (0.29 vs. 1.05 eV for LYG and 0.44 vs. 0.97 eV for XJ). Notably, these values are lower than those typically reported for small polaron conduction (0.6–2.5 eV) and proton conduction (~0.7 eV) in garnets (Dai et al., 2013; Romano et al., 2006). Freer and Edwards (1999) suggested that the diffusion of extrinsic impurities could be pervasive and predominate in silicate garnet. The LYG, XJ megacrysts could incorporate considerable impurities during fractional crystallization. These extrinsic vacancies or impurities have narrower band gap compared to the intrinsic atoms within the minerals lattice, leading to a lower activation energy, as observed in minerals like talc, bridgmanite, and granite (Dai et al., 2014; Guo et al., 2011). Therefore, we propose that an extrinsic mechanism likely governs the electrical conduction of LYG, XJ and their mixture ($LYG_{50}XJ_{50}$) at low temperatures. By contrast, the SD could only incorporate impurity at a low amount, and consequently the conductions of SD and its corresponding mixtures ($LYG_{66}SD_{34}$ and $LYG_{50}SD_{50}$) are governed solely by intrinsic mechanism at both high and low temperatures.

At high temperatures, the dominant conduction mechanism in garnet is likely small polaron conduction, involving the hopping of electron holes between Fe^{3+} and Fe^{2+} cations. For hydrous garnets, protons associated with H^+ defects can become the primary charge carriers (Dai et al., 2012; Dai and Karato, 2009). However, as our garnet samples are nearly anhydrous, this mechanism is not applicable. Dai et al. (2012) reported similar activation energies (1.32–1.37 eV) for the garnet series varying from $Al_{14}Py_{73}Grs_{13}$ to $Al_{76}Py_{20}Grs_4$, suggesting small polaron as a constant conduction mechanism for iron-

bearing garnets. By contrast, Romano et al. (2006) showed that the activation energies of almandine and pyrope vary from 0.6 to 2.5 eV, indicative of a shift in conduction mechanism from small polaron to oxygen vacancies. In our study, the activation energies for single-phase are around 1 eV (Table 2), consistent with the range reported for small polaron conduction. Therefore, it is reasonable to propose that small polaron conduction is the most likely mechanism governing electrical conductivity in our garnet samples.

3.3 Grain Boundary Conductivity

The observed lower conductivity and higher activation energies of the garnet mixtures compared to the single-phase garnets suggest the formation of resistive grain boundaries within the mixtures. The electrical conductivity of a mixture represents the effective value of the combined conductivities of its various constituents. Assuming homogenous distribution and minimal interaction between constituent minerals, the effective conductivity of a mixture can be constrained by various theoretical models (Han and Clark, 2021). Among these, the Hashin-Sthrikman (HS) bounds are considered particularly rigorous (Hashin and Shtrikman, 1963). As shown in Figure 6, the HS bounds predict a range of effective conductivities for the garnet mixtures that lies entirely above the measured values. This discrepancy between measured and modeled conductivities might be attributed to several factors beyond the assumptions of the HS model, such as surface effects, interfacial relaxations, and chemical reactions at grain boundaries (Salje, 2007). Surface effects and interfacial relaxations could play a significant role if a liquid phase was present in the multiphase system (Fenter and Neil, 2004). Alternatively, the chemical gradient between the two garnets could induce interdiffusion of Fe and Mg, leading to the formation of a thin layer of garnet solid solution at the interface. However, such a solid solution would likely exhibit an intermediate conductivity between the constituent endmembers, as observed in feldspar solid solutions where conductivity falls between that of albite and orthoclase (Hu et al., 2013).

Another possibility is the segregation of impurities within the mineral lattice towards the grain boundaries at high temperatures. The grain boundaries in single-phase garnet are interfac-
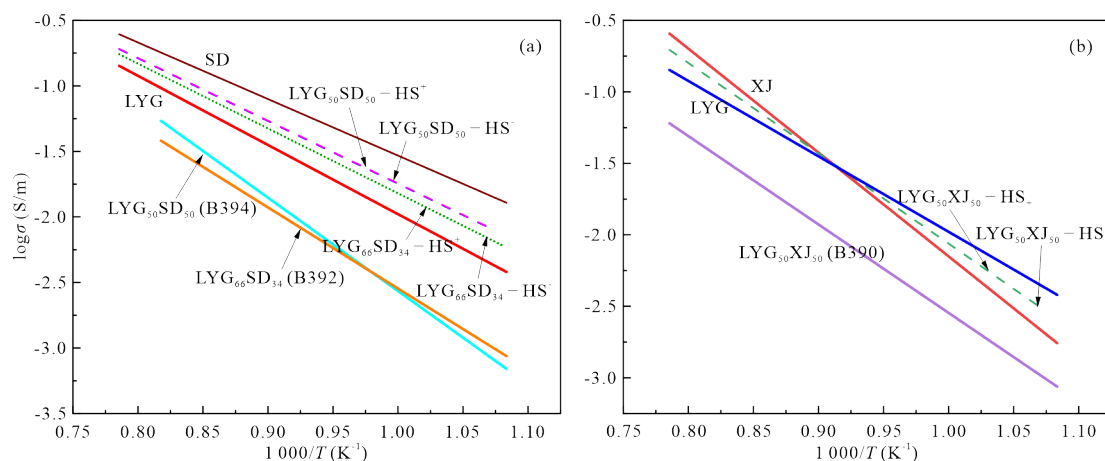

Figure 6. Comparison of the measured electrical conductivity of the mixed-phase garnet samples ($LYG_{50}SD_{50}$ and $LYG_{66}SD_{34}$) with the effective conductivity bounds predicted by the Hashin-Sthrikman (HS) model. The upper HS bound of all mixture in (a) is slightly higher than their lower bound.

es between two grains with identical composition and crystal structure, resembling dislocation arrays. By contrast, for the multiphase counterparts, the grain boundaries at the interface between two garnet phases could comprise an approximately two-dimensional "structural" or "core" region with over ~2-unit cell width, whose atomic structure differs from both adjacent crystals (Vahidi et al., 2021). Since grain boundaries are known to act as sinks for various imperfections such as impurities and vacancies (Shirpour et al., 2012), these wide interphases enable the impurities from the garnet crystals to reside and accumulate at grain boundary core. Also, a three-dimensional space charge zone extends up to several nanometres into the adjacent garnet crystal (Vahidi et al., 2021). In other words, such a zone would be characterized by an impurity-enriched core within the grain boundary and adjacent zones depleted of ions and defects within the lattice (Wang et al., 2020). For instance, incompatible ions in aggregates of olivine and anorthite synthesized at high pressures and temperatures can segregate and enrich at grain boundaries (Hiraga et al., 2004). Compared to garnet lattice, where small polaron conduction dominates, these grain boundaries with segregated ions and depleted zones would be more resistive (Xue et al., 2019; Guo et al., 2002). An interconnected network of such resistive grain boundaries consequently reduces the bulk conductivity of the garnet mixture (Roberts and Tyburczy, 1991). Similar observations of grain boundary conduction due to segregated impurities were reported by Dai et al. (2008) in synthetic peridotite composed of olivine and pyroxene. Additionally, the higher activation energy observed for the mixture compared to the single-phase garnets (Table 2) aligns with the presence of relatively resistive grain boundaries associated with space charge zones, a phenomenon observed in other ceramic materials (Gregori et al., 2017; Gerhardt and Nowick, 1986).

The bulk electrical conductivity of a polycrystalline aggregate can be estimated by combining the contributions of grain interior and grain boundary conductivities. Due to the impeding effect of grain boundary conductivity, the electrical response can be modeled as a series resistor network. The bulk conductivity, σ_t, can therefore be given by the equation according to Roberts and Tyburczy (1999)

$$\sigma_t = 1/(1/\sigma_{gi} + 1/\sigma_{gb}) \qquad (2)$$

where σ_{gb} is the grain boundary conductivity, and σ_{gi} represents the grain interior conductivity. In the case of the garnet mixture, the grain interior conductivity is determined by averaging the Hashin-Shtrikman (HS) bounds, which accounts for the combined conductivity of the individual garnet phases. The derived grain boundary conductivity is the bulk conductivity of grain boundaries at a macro level, encompassing the total contribution from all individually specific grain boundaries within the aggregates. The specific grain boundary conductivity is unable to be measured directly for an aggregate. The equation below shows the relationship between the specific grain boundary conductivity, σ_{gb}^{sp}, and the bulk grain boundary

$$\sigma_{gb} = \sigma_{gb}^{sp} d/\delta \qquad (3)$$

where the grain size (d) and grain boundary thickness (δ) are important factors to be considered. The grain boundaries in the studied material are typically only a few nanometers thick, with a thickness of 1 nm assumed for this analysis (Kiss et al., 2016). The average grain size is approximately 5 μm. The derived bulk grain boundary conductivities of the garnet mixture at macro level are nearly consistent (Figure 7), which are about half order of magnitude lower than the conductivity of grain interior in B394. The bulk grain boundary conductivities obtained for the garnet mixture are comparable to those reported for natural andesite (Hui et al., 2015). However, they are approximately one order of magnitude higher than the values observed in synthetic peridotite (Dai et al., 2008). Given the distinct grain size (50 μm) of the synthetic peridotite from our study (~5 μm), this observed discrepancy in bulk grain boundary conductivity suggests a potential influence of the specific grain boundary at the microscopic level, as predicted by Eq. (3).

The activation energies of grain boundary conduction are higher than the single-phase garnet (Table 3), supporting the impeding effects of grain boundary conduction on the bulk conductivity of the garnet mixture. The activation energies of grain boundary conduction vary within a wide range (1.17–1.55 eV), which are comparable to that of synthetic peridotite (1.32–1.45 eV) (Dai et al. 2008). The activation energies are higher than natural andesite (~0.9 eV) but much lower than those in olivine compact (2.47 eV) and scandia-doped zirconia polycrystals (2.143 eV) (Xue et al., 2019; Hui et al., 2015; Roberts and Tyburczy, 1991). The considerable variation in activation energy of grain boundary conduction could be dependent on several factors including species of charge carriers, their mobility and concentration, the structure of grain boundaries, presence of water or fluid and oxygen fugacity (Gregori et al., 2017; Kiss et al., 2016; Gasc et al., 2011; Dai et al., 2008). Identifying and
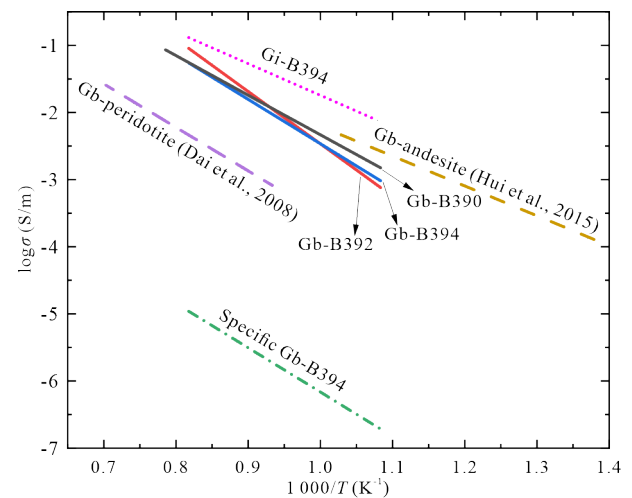

Figure 7. The comparison of grain boundary and grain interior conductivity. The solid lines are the grain boundary conductivity at macro level. The dotted line is the grain interior conductivity of B394.

Table 3 Fitted Arrhenius parameters of grain boundary conductivity

Run	σ_0 (kS/m)	ΔH (eV)
B390	3.66	1.17
B392	214.19	1.55
B394	13.66	1.31

quantifying the exact charge carriers and their concentrations involved in conduction at grain boundaries and the adjacent grain rim region remains a significant technical challenge (Peng et al., 2022; Vahidi et al., 2021).

4 GEOLOGICAL IMPLICATIONS

The grain boundary conductivity could affect the electrical conductivity of garnet-bearing rocks at diverse geological settings. The interaction between subducted plate of oceanic lithosphere and the ambient mantle is a major process of mantle mixing and homogenization (van Keken et al., 2002). However, observations of electrical conductivity anomalies associated with subducted slabs in the MTZ reveal contrasting behavior (Kelbert et al., 2009). Stagnant slabs beneath southern Europe exhibit lower conductivity compared to the ambient mantle (Fukao et al., 2009; Tarits et al., 2004), while the slabs in the MTZ under northeastern China display higher conductivity than their neighboring mantle regions (Zhang et al., 2020; Huang and Zhao, 2006). These contrasting conductivity patterns could be attributed to the influence of grain boundary conductivity between garnets with varying compositions. Garnets formed from mid-ocean ridge basalts (MORB) are typically enriched in the grossular component, while those in peridotite are usually composed of approximately 75% pyrope, 10% grossular, and 15% almandine (Wood et al., 2013). The abundance of majorite garnet increases significantly within the MTZ, reaching 90% in MORB and 40% in pyrolite (Irifune and Tsuchiya, 2007). This suggests potential mixing between MORB garnet in stagnant slabs and pyrolite garnet in the ambient mantle,
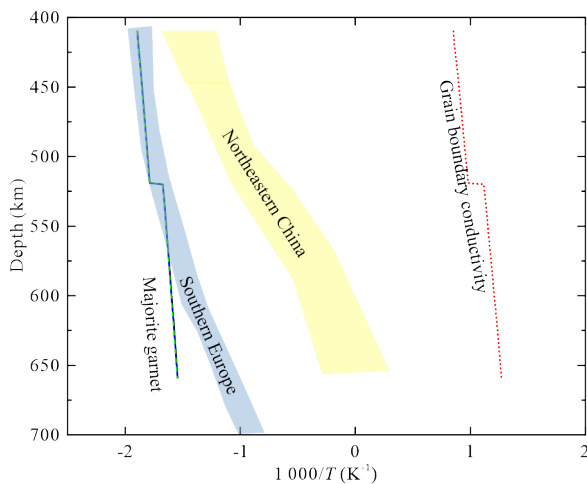

Figure 8. Conductivity profile of majorite garnet mixture in the mantle transition zone. This figure depicts the calculated conductivity profile of a majorite garnet mixture within the mantle transition zone (MTZ) at depths ranging from 410 to 660 km. The green dashed line represents the intrinsic conductivity of dry majorite garnet, based on the model by Yoshino et al. (2008). The blue solid line represents the bulk conductivity of the majorite mixture, which incorporates both grain boundary and majorite garnet conductivity. Notably, the calculated bulk conductivity profile closely resembles the intrinsic conductivity of dry majorite garnet. The temperature profile within the stagnant slabs (not shown), assumed to be 300 K lower than the adiabatic temperature profile (adopted from Katsura, 2022), is used in the conductivity calculations.

leading to the formation of grain boundaries. The slow rate of ion diffusion within garnet hinders the efficient mixing of these distinct garnet compositions, thereby contributing to the long-term persistence of grain boundary conductivity within the MTZ (Holzapfel et al., 2005).

Majorite, as one type of garnet, is assumed to have equivalent concentration and mobility of charge carriers, as well as the overall grain boundary structure to the garnet aggregates in our study. Based on this assumption, a previously established laboratory-based conductivity model for dry majorite garnet (Yoshino et al., 2008) is employed to estimate the conductivity within the mantle transition zone (MTZ). Pressure is considered insignificant in modeling the grain boundary conductivity (Gregori et al., 2017). The estimated surface temperature of stagnant slabs is considered to be 300–400 K below the adiabatic temperature (Schmid et al., 2006). Additionally, friction during subduction is expected to induce a grain size of approximately 100 μm for majorite on the slab surface (Wada et al., 2011). Notably, the grain boundary conductivity calculated using the parameters for B394 (Table 3) is found to be two orders of magnitude higher than that of majorite itself (Figure 8). In light of these considerations, a cube model comprising cubic grains and conductive grain boundary films is chosen for calculating the bulk conductivity of a majorite mixture within the MTZ (Waff, 1974). The formula of cube model is presented as follows

$$\sigma_t = \frac{\sigma_{gi}\sigma_{gb}\left(1 - X_{gb}\right)^{\frac{2}{3}}}{\sigma_{gb}\left(1 - X_{gb}\right)^{\frac{2}{3}} + \sigma_{gi}\left[1 - \left(1 - X_{gb}\right)^{\frac{1}{3}}\right]} +$$
$$\sigma_{gi}\left[1 - \left(1 - X_{gb}\right)^{\frac{2}{3}}\right] \tag{4}$$

and X_{gb} the volume fraction of grain boundaries, is calculated by

$$X_{gb} = \frac{\left(d + \delta\right)^3 - d^3}{\left(d + \delta\right)^3} \tag{5}$$

where d and δ are the grain size and grain boundary thickness, respectively.

The bulk conductivity of majorite mixture is only slightly higher than that of its constituent majorite, suggesting a limited impact of grain boundary on the bulk conductivity of a mantle rock. For stagnant slabs in southern Europe, located shallower than 570 km (Tarits et al., 2004), their low electrical conductivity can likely be attributed to the presence of dry majorite. However, if the stagnant slab is more than 300 K colder than the ambient mantle (Schmid et al., 2006), it is also possible that the majorite could contain a certain amount of structural water. Nevertheless, this interpretation suggests that the observed conductivity anomaly might not necessarily require the additional influence of grain boundary conductivity.

In contrast, the highly conductive anomaly observed in the slab beneath northeastern China (Zhang et al., 2020) may require the presence of a certain amount of water. However, there is a lack of clear understanding of the relationship between water content and conductivity in majorite. This highlights the need for future research to determine the precise water content within majorite in these settings. Despite the limited impact observed in our model, it is crucial to consider the potential influence of grain boundary conductivity when interpret-

ing magnetotelluric and/or geomagnetic observations using electrical conductivity models.

ACKNOWLEDGMENTS

Electronic Supplementary Materials: Supplementary materials (Figures S1–S2, Table S1) are available in the online version of this article athttps://doi. org/10.1007/s12583-024-0062-8.

Conflict of Interest

The authors declare that they have no conflict of interest.

REFERENCES CITED

Amulele, G. M., Lanati, A. W., Clark, S. M., 2022. The Electrical Conductivity of Albite Feldspar: Implications for Oceanic Lower Crustal Sequences and Subduction Zones. *American Mineralogist*, 107(4): 614–624. https://doi.org/10.2138/am-2021-7836

Bell, D. R., Ihinger, P. D., Rossman, G. R., 1995. Quantitative Analysis of Trace OH in Garnet and Pyroxenes. *American Mineralogist*, 80(5/6): 465–474. https://doi.org/10.2138/am-1995-5-607

Dachs, E., 2006. Heat Capacities and Entropies of Mixing of Pyrope-Grossular ($Mg_3Al_2Si_3O_{12}$-$Ca_3Al_2Si_3O_{12}$) Garnet Solid Solutions: A Low-Temperature Calorimetric and a Thermodynamic Investigation. *American Mineralogist*, 91(5/6): 894–906. https://doi.org/10.2138/am.2006.2005

Dai, L. D., Karato, S. I., 2009. Electrical Conductivity of Wadsleyite at High Temperatures and High Pressures. *Earth and Planetary Science Letters*, 287(1/2): 277–283. https://doi.org/10.1016/j.epsl.2009.08.012

Dai, L. D., Li, H. P., Hu, H. Y., et al., 2008. Experimental Study of Grain Boundary Electrical Conductivities of Dry Synthetic Peridotite under High-Temperature, High-Pressure, and Different Oxygen Fugacity Conditions. *Journal of Geophysical Research*: *Solid Earth*, 113(B12): B12211. https://doi.org/10.1029/2008jb005820

Dai, L. D., Li, H. P., Hu, H. Y., et al., 2012. The Effect of Chemical Composition and Oxygen Fugacity on the Electrical Conductivity of Dry and Hydrous Garnet at High Temperatures and Pressures. *Contributions to Mineralogy and Petrology*, 163(4): 689–700. https://doi.org/10.1007/s00410-011-0693-5

Dai, L. D., Li, H. P., Hu, H. Y., et al., 2013. Electrical Conductivity of $Alm_{82}Py_{15}Grs_3$ Almandine-Rich Garnet Determined by Impedance Spectroscopy at High Temperatures and High Pressures. *Tectonophysics*, 608: 1086–1093. https://doi.org/10.1016/j.tecto.2013.07.004

Dai, L. D., Hu, H. Y., Li, H. P., et al., 2014. Influence of Temperature, Pressure, and Chemical Composition on the Electrical Conductivity of Granite. *American Mineralogist*, 99(7): 1420–1428. https://doi.org/10.2138/am.2014.4692

Farla, R. J. M., Peach, C. J., Ten Grotenhuis, S. M., 2010. Electrical

Conductivity of Synthetic Iron-Bearing Olivine. *Physics and Chemistry of Minerals*, 37(3): 167–178. https://doi.org/10.1007/s00269-009-0321-3

Feng, B., Guo, X. Z., 2022. Thermal Conductivity and Thermal Diffusivity of Ferrosilite under High Temperature and High Pressure. *Journal of Earth Science*, 33(3): 770–777. https://doi.org/10.1007/s12583-021-1574-0

Fenter, P., Sturchio, N. C., 2004. Mineral-Water Interfacial Structures Revealed by Synchrotron X-Ray Scattering. *Progress in Surface Science*, 77(5/6/7/8): 171–258. https://doi.org/10.1016/j.progsurf.2004.12.001

Freer, R., Edwards, A., 1999. An Experimental Study of Ca- (Fe, Mg) Interdiffusion in Silicate Garnets. *Contributions to Mineralogy and Petrology*, 134(4): 370–379. https://doi.org/10.1007/s004100050491

Fukao, Y., Obayashi, M., Nakakuki, T., 2009. Stagnant Slab: A Review. *Annual Review of Earth and Planetary Sciences*, 37: 19–46. https://doi.org/10.1146/annurev.earth.36.031207.124224

Gasc, J., Brunet, F., Bagdassarov, N., et al., 2011. Electrical Conductivity of Polycrystalline $Mg(OH)_2$ at 2 GPa: Effect of Grain Boundary Hydration-Dehydration. *Physics and Chemistry of Minerals*, 38(7): 543–556. https://doi.org/10.1007/s00269-011-0426-3

Geiger, C. A., Rossman, G. R., 2018. IR Spectroscopy and OH^- in Silicate Garnet: The Long Quest to Document the Hydrogarnet Substitution. *American Mineralogist*, 103(3): 384–393. https://doi.org/10.2138/am-2018-6160ccby

Gerhardt, R., Nowick, A. S., 1986. Grain-Boundary Effect in Ceria Doped with Trivalent Cations: I, Electrical Measurements. *Journal of the American Ceramic Society*, 69(9): 641–646. https://doi.org/10.1111/j.1151-2916.1986.tb07464.x

Gregori, G., Merkle, R., Maier, J., 2017. Ion Conduction and Redistribution at Grain Boundaries in Oxide Systems. *Progress in Materials Science*, 89: 252–305. https://doi.org/10.1016/j.pmatsci.2017.04.009

Guo, X., Sigle, W., Fleig, J., et al., 2002. Role of Space Charge in the Grain Boundary Blocking Effect in Doped Zirconia. *Solid State Ionics*, 154/155: 555–561. https://doi.org/10.1016/s0167-2738(02)00491-5

Guo, X. Z., Yoshino, T., Katayama, I., 2011. Electrical Conductivity Anisotropy of Deformed Talc Rocks and Serpentinites at 3 GPa. *Physics of the Earth and Planetary Interiors*, 188(1): 69–81. https://doi.org/10.1016/j.pepi.2011.06.012

Han, K., Clark, S. M., 2021. Review of Calculating the Electrical Conductivity of Mineral Aggregates from Constituent Conductivities. *Solid Earth Sciences*, 6(2): 111–128. https://doi.org/10.1016/j.sesci.2021.02.003

Han, K., Guo, X. Z., Zhang, J. F., et al., 2021. Fast Grain-Boundary Ionic Conduction in Multiphase Aggregates as Revealed by Electrical Conductivity Measurements. *Contributions to Mineralogy and Petrology*, 176(10): 80. https://doi.org/10.1007/s00410-021-01841-1

Hashin, Z., Shtrikman, S., 1963. A Variational Approach to the Theory of the Elastic Behaviour of Multiphase Materials. *Journal of the Mechanics and Physics of Solids*, 11(2): 127–140. https://doi.org/10.1016/0022-5096(63)90060-7

Hiraga, T., Anderson, I. M., Kohlstedt, D. L., 2004. Grain Boundaries as Reservoirs of Incompatible Elements in the Earth's Mantle. *Nature*, 427(6976): 699–703. https://doi.org/10.1038/nature02259

Holzapfel, C., Rubie, D. C., Frost, D. J., et al., 2005. Fe-Mg Interdiffusion in (Mg, Fe)SiO_3 Perovskite and Lower Mantle Reequilibration. *Science*, 309(5741): 1707–1710. https://doi.org/10.1126/science.1111895

Hu, H. Y., Li, H. P., Dai, L. D., et al., 2013. Electrical Conductivity of Alkali Feldspar Solid Solutions at High Temperatures and High

Pressures. *Physics and Chemistry of Minerals*, 40(1): 51–62. https://doi.org/10.1007/s00269-012-0546-4

Huang, J. L., Zhao, D. P., 2006. High-Resolution Mantle Tomography of China and Surrounding Regions. *Journal of Geophysical Research*: *Solid Earth*, 111(B9): B09305. https://doi.org/10.1029/2005jb004066

Hui, K. S., Zhang, H., Li, H. P., et al., 2015. Experimental Study on the Electrical Conductivity of Quartz Andesite at High Temperature and High Pressure: Evidence of Grain Boundary Transport. *Solid Earth*, 6(3): 1037–1043. https://doi.org/10.5194/se-6-1037-2015

Irifune, T., Tsuchiya, T., 2007. Mineralogy of the Earth—Phase Transitions and Mineralogy of the Lower Mantle. Treatise on Geophysics. Elsevier, Amsterdam. 33–62. https://doi.org/10.1016/b978-044452748-6/00030-4

Katsura, T., 2022. A Revised Adiabatic Temperature Profile for the Mantle. *Journal of Geophysical Research*: *Solid Earth*, 127(2): e2021JB023562. https://doi.org/10.1029/2021jb023562

Kelbert, A., Schultz, A., Egbert, G., 2009. Global Electromagnetic Induction Constraints on Transition-Zone Water Content Variations. *Nature*, 460(7258): 1003–1006. https://doi.org/10.1038/nature08257

Keppler, H., Rauch, M., 2000. Water Solubility in Nominally Anhydrous Minerals Measured by FTIR and 1H MAS NMR: The Effect of Sample Preparation. *Physics and Chemistry of Minerals*, 27(6): 371–376. https://doi.org/10.1007/s002699900070

Kiss, Á. K., Rauch, E. F., Lábár, J. L., 2016. Highlighting Material Structure with Transmission Electron Diffraction Correlation Coefficient Maps. *Ultramicroscopy*, 163: 31–37. https://doi.org/10.1016/j.ultramic.2016.01.006

Li, X., Liu, L., Liao, X. Y., et al., 2023. Metamorphic Evolution of Garnet Amphibolite from the Yaganbuyang Area in the South Altyn Orogen, West China: Insights from Phase Equilibria Modeling and Geochronology. *Journal of Earth Science*, 34(3): 640–657. https://doi.org/10.1007/s12583-021-1439-6

Linckens, J., Tholen, S., 2021. Formation of Ultramylonites in an Upper Mantle Shear Zone, Erro-Tobbio, Italy. *Minerals*, 11(10): 1036. https://doi.org/10.3390/min11101036

Liu, H. Y., Yang, X. Z., Karato, S. I., 2023. Small Effect of Partial Melt on Electrical Anomalies in the Asthenosphere. *Science Advances*, 9(13): eabq7884. https://doi.org/10.1126/sciadv.abq7884

Liu, H. Y., Zhu, Q., Yang, X. Z., 2019. Electrical Conductivity of OH-Bearing Omphacite and Garnet in Eclogite: The Quantitative Dependence on Water Content. *Contributions to Mineralogy and Petrology*, 174(7): 57. https://doi.org/10.1007/s00410-019-1593-3

Liu, J., Yuan, L. L., Yang, Z. L., 2022. Geochronology and Geochemistry of Mesozoic Mafic Intrusive Rocks in Zhongtiao Mountain Area: Characterizing Lithospheric Mantle of Southern North China Craton. *Earth Science*, 47(4): 1271–1294. https://doi.org/10.3799/dqkx.2021.104 (in Chinese with English Abstract)

Luo, X., Xia, Q. X., Zheng, Y. F., et al., 2022. An Experimental Study of Partial Melting of Metafelsic Rocks: Constraints on the Feature of Anatectic Melts and the Origin of Garnets in Collisional Orogens. *Journal of Earth Science*, 33(3): 753–769. https://doi.org/10.1007/s12583-021-1547-3

Marquardt, K., Faul, U. H., 2018. The Structure and Composition of Olivine Grain Boundaries: 40 Years of Studies, Status and Current Developments. *Physics and Chemistry of Minerals*, 45(2): 139–172. https://doi.org/10.1007/s00269-017-0935-9

Nagurney, A. B., Caddick, M. J., Pattison, D. R. M., et al., 2021. Preferred Orientations of Garnet Porphyroblasts Reveal Previously Cryptic

Templating during Nucleation. *Scientific Reports*, 11: 6869. https://doi.org/10.1038/s41598-021-85525-7

Peng, Z. R., Meiners, T., Lu, Y. F., et al., 2022. Quantitative Analysis of Grain Boundary Diffusion, Segregation and Precipitation at a Sub-Nanometer Scale. *Acta Materialia*, 225: 117522. https://doi.org/10.1016/j.actamat.2021.117522

Pommier, A., Kohlstedt, D. L., Hansen, L. N., et al., 2018. Transport Properties of Olivine Grain Boundaries from Electrical Conductivity Experiments. *Contributions to Mineralogy and Petrology*, 173(5): 41. https://doi.org/10.1007/s00410-018-1468-z

Roberts, J. J., Tyburczy, J. A., 1991. Frequency Dependent Electrical Properties of Polycrystalline Olivine Compacts. *Journal of Geophysical Research*: *Solid Earth*, 96(B10): 16205–16222. https://doi.org/10.1029/91jb01574

Roberts, J. J., Tyburczy, J. A., 1999. Partial-Melt Electrical Conductivity: Influence of Melt Composition. *Journal of Geophysical Research*: *Solid Earth*, 104(B4): 7055–7065. https://doi.org/10.1029/1998jb900111

Romano, C., Poe, B. T., Kreidie, N., et al., 2006. Electrical Conductivities of Pyrope-Almandine Garnets up to 19 GPa and 1 700 °C. *American Mineralogist*, 91(8/9): 1371–1377. https://doi.org/10.2138/am.2006.1983

Salje, E. K. H., 2007. An Empirical Scaling Model for Averaging Elastic Properties Including Interfacial Effects. *American Mineralogist*, 92(2/3): 429–432. https://doi.org/10.2138/am.2007.2472

Schmid, C., van der Lee, S., Giardini, D., 2006. Correlated Shear and Bulk Moduli to 1 400 km beneath the Mediterranean Region. *Physics of the Earth and Planetary Interiors*, 159(3/4): 213–224. https://doi.org/10.1016/j.pepi.2006.07.003

Shirpour, M., Rahmati, B., Sigle, W., et al., 2012. Dopant Segregation and Space Charge Effects in Proton-Conducting $BaZrO_3$ Perovskites. *The Journal of Physical Chemistry C*, 116(3): 2453–2461. https://doi.org/10.1021/jp208213x

Stixrude, L., Lithgow-Bertelloni, C., 2012. Geophysics of Chemical Heterogeneity in the Mantle. *Annual Review of Earth and Planetary Sciences*, 40(1): 569–595. https://doi.org/10.1146/annurev.earth.36.031207.124244

Tarits, P., Hautot, S., Perrier, F., 2004. Water in the Mantle: Results from Electrical Conductivity beneath the French Alps. *Geophysical Research Letters*, 31(6): L06612. https://doi.org/10.1029/2003gl019277

Vahidi, H., Syed, K., Guo, H. M., et al., 2021. A Review of Grain Boundary and Heterointerface Characterization in Polycrystalline Oxides by (Scanning) Transmission Electron Microscopy. *Crystals*, 11(8): 878. https://doi.org/10.3390/cryst11080878

van Keken, P. E., Hauri, E. H., Ballentine, C. J., 2002. Mantle Mixing: The Generation, Preservation, and Destruction of Chemical Heterogeneity. *Annual Review of Earth and Planetary Sciences*, 30: 493–525. https://doi.org/10.1146/annurev.earth.30.091201.141236

Wada, I., Behn, M. D., He, J. H., 2011. Grain-Size Distribution in the Mantle Wedge of Subduction Zones. *Journal of Geophysical Research*: *Solid Earth*, 116(B10): B10203. https://doi.org/10.1029/2011jb008294

Waff, H. S., 1974. Theoretical Considerations of Electrical Conductivity in a Partially Molten Mantle and Implications for Geothermometry. *Journal of Geophysical Research*, 79(26): 4003–4010. https://doi.org/10.1029/jb079i026p04003

Wang, D. J., Yu, Y. J., Zhou, Y. S., 2014. Electrical Conductivity Anisotropy in Alkali Feldspar at High Temperature and Pressure. *High Pressure Research*, 34(3): 297–308. https://doi.org/10.1080/08957959.2014.913042

Wang, W. Z., Xu, Y. H., Sun, D. Y., et al., 2020. Velocity and Density

Characteristics of Subducted Oceanic Crust and the Origin of Lower-Mantle Heterogeneities. *Nature Communications*, 11: 64. https://doi.org/10.1038/s41467-019-13720-2

Wood, B. J., Kiseeva, E. S., Matzen, A. K., 2013. Garnet in the Earth's Mantle. *Elements*, 9(6): 421–426. https://doi.org/10.2113/gselements.9.6.421

Xu, Y. S., Shankland, T. J., 1999. Electrical Conductivity of Orthopyroxene and Its High Pressure Phases. *Geophysical Research Letters*, 26(17): 2645–2648. https://doi.org/10.1029/1999gl008378

Xue, Q. N., Huang, X. W., Zhang, J. X., et al., 2019. Grain Boundary Segregation and Its Influences on Ionic Conduction Properties of Scandia Doped Zirconia Electrolytes. *Journal of Rare Earths*, 37(6): 645–651. https://doi.org/10.1016/j.jre.2018.11.006

Yang, X. Z., McCammon, C., 2012. Fe^{3+}-Rich Augite and High Electrical Conductivity in the Deep Lithosphere. *Geology*, 40(2): 131–134. https://doi.org/10.1130/g32725.1

Yoshino, T., Nishi, M., Matsuzaki, T., et al., 2008. Electrical Conductivity of Majorite Garnet and Its Implications for Electrical Structure in the Mantle Transition Zone. *Physics of the Earth and Planetary Interiors*, 170(3/4): 193–200. https://doi.org/10.1016/j.pepi.2008.04.009

Yoshino, T., Shimojuku, A., Shan, S. M., et al., 2012. Effect of Temperature, Pressure and Iron Content on the Electrical Conductivity of Olivine and Its High-Pressure Polymorphs. *Journal of Geophysical Research*: *Solid Earth*, 117(B8): 102. https://doi.org/10.1029/2011jb008774

Yu, P. P., Ding, W., Zeng, C. Y., et al., 2023. Episodic Magmatism and Continental Reworking in the Yunkai Domain, South China. *Earth Science*, 48(9): 3205–3220. https://doi.org/10.3799/dqkx.2023.078 (in Chinese with English Abstract)

Zhang, B. H., Yoshino, T., 2016. Effect of Temperature, Pressure and Iron Content on the Electrical Conductivity of Orthopyroxene. *Contributions to Mineralogy and Petrology*, 171(12): 102. https://doi.org/10.1007/s00410-016-1315-z

Zhang, B. H., Yoshino, T., Zhao, C. C., 2019. The Effect of Water on Fe-Mg Interdiffusion Rates in Ringwoodite and Implications for the Electrical Conductivity in the Mantle Transition Zone. *Journal of Geophysical Research*: *Solid Earth*, 124(3): 2510–2524. https://doi.org/10.1029/2018jb016415

Zhang, J., Chen, X. B., Yin, X. K., et al., 2022. 3-D AMT Array Exploration in the Selaha Fault and Adjacent Area. *Earth Science*, 47(3): 856–866. https://doi.org/10.3799/dqkx.2022.060 (in Chinese with English Abstract)

Zhang, X. B., Zhang, P. H., He, M. X., et al., 2023. Crustal Electrical Structure of the Wuwei Basin, Lower Yangtze Region of China, and Its Geological Implications. *Journal of Earth Science*, 34(6): 1744–1757. https://doi.org/10.1007/s12583-022-1682-5

Zhang, Y. H., Weng, A. H., Li, S. W., et al., 2020. Electrical Conductivity in the Mantle Transition Zone beneath Eastern China Derived from L1-Norm C-Responses. *Geophysical Journal International*, 221(2): 1110–1124. https://doi.org/10.1093/gji/ggaa059

Zhou, C. A., Song, S. G., 2023. Post-Collision Magmatism and Continental Crust Growth in Continental Orogenic Belt: An Example from North Qaidam Ultrahigh-Pressure Metamorphic Belt. *Earth Science*, 48(12): 4481–4494. https://doi.org/10.3799/dqkx.2022.117 (in Chinese with English Abstract)